In Situ Plasma Studies Using a Direct Current Microplasma in a Scanning Electron Microscope

*Lukas Grünewald, Dmitry Chezganov, Robin De Meyer, Andrey Orekhov, Sandra Van Aert, Annemie Bogaerts, Sara Bals, and Jo Verbeeck**

Microplasmas can be used for a wide range of technological applications and to improve the understanding of fundamental physics. Scanning electron microscopy, on the other hand, provides insights into the sample morphology and chemistry of materials from the mm- down to the nm-scale. Combining both would provide direct insight into plasma-sample interactions in real-time and at high spatial resolution. Up till now, very few attempts in this direction have been made, and significant challenges remain. This work presents a stable direct current glow discharge microplasma setup built inside a scanning electron microscope. The experimental setup is capable of real-time in situ imaging of the sample evolution during plasma operation and it demonstrates localized sputtering and sample oxidation. Further, the experimental parameters such as varying gas mixtures, electrode polarity, and field strength are explored and experimental *V–I* curves under various conditions are provided. These results demonstrate the capabilities of this setup in potential investigations of plasma physics, plasma-surface interactions, and materials science and its practical applications. The presented setup shows the potential to have several technological applications, for example, to locally modify the sample surface (e.g., local oxidation and ion implantation for nanotechnology applications) on the µm-scale.

1. Introduction

Plasma is a complex and versatile state of matter with many established applications, for example, in the semiconductor industry,[1] as well as promising emerging technologies. The potential of plasma technology spans a broad range, including biomedical applications,[2] materials science,[3] and gas conversion for environmental applications.[4] Many different types of plasma exist,[5] but the simplest geometry consists of two electrodes separated by a gas (at low, atmospheric, or elevated pressure), with a voltage being applied between the electrodes.[6] More recently, so-called "microplasmas" have received a rising interest in the scientific community.[7–11] Microplasmas have at least one dimension in the sub-mm range.[8] Besides the: i) practical aspect of reduced operation cost of microplasma setups compared to large plasma reactors for laboratory-scale experiments and ii) a general trend toward miniaturization of devices in plasma-application areas, microplasmas also have interesting properties. For example, the large surface-to-volume ratio and short gap distances between the electrodes (typically a few 100 µm) lead to a non-equilibrium state where the ion/gas temperature is lower than the electron temperature.[3] This results in a "cold" plasma with gas temperatures close to room temperature,[7–9] which shows great promise, for example, in nanomaterial and nanoparticle fabrication.[3] In addition, microplasmas are not confined to vacuum operation. Paschen's law relates the breakdown voltage of a gas with the product pd of the pressure p and the gap distance d between two parallel electrode plates. For many gases, the smallest breakdown voltages lie in the range of about 10 to 1000 Pa cm.[9] Reducing d to 100 µm or less allows plasma operation at or near atmospheric pressure ($p = 101$ kPa).

The plasma setup presented in this work is a direct current (DC) microplasma where one of the electrodes is a nozzle with a small orifice through which gas is supplied (see Figure 9a in the Experimental Section). Whereas the geometry closely resembles that of a jet, the setup is not technically defined as a plasma jet since the plasma is generated in the gap between the nozzle and the grounded electrode/sample.[12] The interaction of plasmas with flat surfaces or nanoparticles is of interest for technical applications and a better understanding of plasma physics and chemistry. Often, ex situ structural and chemical investigations

L. Grünewald, D. Chezganov, R. De Meyer, A. Orekhov, S. Van Aert,
S. Bals, J. Verbeeck
EMAT
University of Antwerp
Groenenborgerlaan 171, Antwerp B-2020, Belgium
E-mail: jo.verbeeck@uantwerpen.be

D. Chezganov, R. De Meyer, S. Van Aert, S. Bals
NANOlab Center of Excellence
University of Antwerp
Groenenborgerlaan 171, Antwerp B-2020, Belgium

R. De Meyer, A. Bogaerts
PLASMANT
University of Antwerp
Universiteitsplein 1, Antwerpen-Wilrijk B-2610, Belgium

The ORCID identification number(s) for the author(s) of this article can be found under https://doi.org/10.1002/admt.202301632

DOI: 10.1002/admt.202301632

on the milli- to nanometer scale are performed after plasma treatment of a material.

For these length scales, scanning electron microscopy is a valuable technique for microstructural and chemical investigations (typically using energy-dispersive X-ray spectroscopy, EDS). Recently, the first microplasmas were generated inside scanning electron microscopes (SEMs).[13–15] A plasma-in-SEM setup not only reduces the time between plasma treatment and subsequent SEM analyses compared to a separate plasma setup, but also prevents exposure of the sample surface to ambient air. The latter aspect enables studies of plasma-treated surfaces where subsequent contact with oxygen, humidity, or contamination must be avoided.

Different approaches to generate plasmas in SEMs were demonstrated in earlier studies. For example, local sputter etching was achieved by Mulders and Trompenaars[14] by introducing a small gas nozzle into an SEM and using the electron beam for ionization. In the setup by these authors, the electron beam is scanned in a small slit in the nozzle near the orifice to generate ions in the gas stream. The generated ions flow out of the orifice with the gas flow and are then accelerated toward the sample using an applied voltage between the nozzle and the stage. Modern SEMs often have a built-in option to apply the required negative voltage to the sample stage, typically used for beam-deceleration SEM imaging.[16,17] This approach does not require reaching the breakdown voltage of the gas, hence leading to a low-energy ion bombardment of the sample. With this setup, low-energy Ar^+ ions with energies ranging from 20 to 500 eV were used to remove amorphous surface layers.[18,19]

Another plasma setup consists of a micro hollow cathode (or anode) DC plasma configuration in an environmental SEM (ESEM).[15] In the latter, the chamber pressure and gas type (in this case, Ar) are directly controlled by the ESEM. A supplied high voltage (in this case, ±1 kV) generates the plasma, and the plasma-surface interaction subsequently can be analyzed within the ESEM. Depending on the electrode polarity, either: i) redeposition of sputtered material from the counter electrode onto the sample surface or ii) direct sputtering of the sample surface with positive ions was observed. The sputtered area had a relatively large width of about 2 mm.[15] A benefit of this experimental setup is that the gas-flow controls of the ESEM are used, which reduces the requirements for the hardware modifications to an SEM. However, a drawback is that using the low-vacuum mode reduces the image quality due to electron-beam scattering in the gas, resulting in a so-called electron-beam skirt.[20,21] This aspect impedes in situ SEM imaging of the plasma-sample interactions, limiting high-quality imaging to the normal high-vacuum mode of the ESEM. To optimize image quality in gaseous environments, the distance between the end of the microscope's pole piece and the sample, that is, the gas-path length, is typically minimized to reduce the beam skirt. However, the gas-path length cannot be reduced too much for plasma experiments due to the risk of unwanted arcing to the microscope hardware. Indeed, arcing from the micro hollow cathode to the microscope hardware over a relatively large distance of about 25 mm was reported for this setup using the low-vacuum mode.[15]

Matra et al.[13,22,23] demonstrated a working jet-like microplasma setup inside an SEM. This approach combines the properties of a jet (enabling a comparably high pressure in the gas jet compared to its environment) with the small dimensions of a microplasma for local plasma application (typically within a few 10 µm). The gas flows from a gas nozzle with a small orifice (nominal diameter of a few 10 µm) toward a (flat) sample surface, whereas the chamber is continuously pumped to maintain a low overall pressure. Plasma is generated by applying a voltage, here denoted as source voltage V_S, between the nozzle and the sample, somewhat similar to a plasma reactor with two electrode plates.[6] However, the non-uniform pressure profile between the nozzle and the sample makes this plasma configuration unique, complicating the characterization of the plasma discharge. The gap distance can be adjusted by using SEM imaging for alignment. The pressure profile between the nozzle and the sample can be modified by changing the gas flow, though it will also be heavily affected by the distance between the orifice and the sample. A plasma is generated by applying at least the breakdown voltage between the nozzle and the sample (although the electron beam can be used to aid plasma ignition). Depending on the gas, material removal by Ar^+ sputtering[13] and the growth of a C-rich thin film[24] on a Si surface were observed. This proof-of-principle study[13] showed that a microplasma jet can be generated in the evacuated SEM chamber.

However, the (desired) DC glow discharge was reported not to be fully stable, resulting in arcing to the sample[13] and a self-pulsing plasma mode for discharge currents in the range of about 3 to 30 µA (depending on voltage, gas flow rate, and gap distance).[22] This arcing led to strong local heating and pronounced damaged spots on the sample.[13] Furthermore, these previous studies did not investigate the possibility of "true" in situ SEM imaging, that is, live SEM imaging during plasma operation. Instead, SEM images were taken before and after the plasma-treatment steps (also in ref. [15]), which will be denoted as "quasi" in situ operation in this work. Still, these studies prove that a microplasma can be generated in an SEM and used for surface treatment. This provides the opportunity to observe in situ changes of a sample's morphology and chemistry on the mm to nm scale during plasma treatment using an SEM, ultimately leading to a better understanding of plasma-surface interactions and fundamental plasma properties.

However, the availability of more studies is hampered by (1) the required non-trivial modifications of an SEM and (2) the lack of commercial solutions. In this work, a microplasma setup built inside a modern ESEM based on the work of Matra et al.[13] is presented. A stable operation of a DC discharge without arcing is realized. Further, we present real-time in situ SEM imaging during plasma operation and show exemplary applications of our plasma-in-SEM setup for sputtering and local surface oxidation. Finally, experimental challenges and potential upgrades to the setup are discussed.

2. Results and Discussion

The first part of this section shows results related to the microplasma and in situ SEM imaging. The second part discusses some exemplary results when applying the microplasma to materials. Finally, the third part reviews the limitations of this setup and proposes potential solutions to overcome these limitations.

2.1. Microplasma Characterization

2.1.1. Gas-Pressure Profile

The used plasma setup has a non-uniform gas pressure along the plasma gap. The gas density profile can be visualized by SEM imaging (**Figure 1**) by using a low primary electron energy (here 2 keV) to increase the electron-scattering probability and secondary electron (SE) generation within the gas cloud.[25] As a result, the SE-SEM image presumably shows higher intensity in regions with higher gas densities (Figure 1a). Here, the gas cloud in Figure 1a flows into the microscope vacuum without obstruction. The contrast variations in the background result from out-of-focus imaging of the sample stage a few mm below the nozzle along the electron-beam direction. The gas density is highest close to the orifice and gradually decreases away from it. This monotonic decrease is in accordance with calculated gas density profiles of restricted gas flows, for example, in refs. [26–28]. More explicitly, Salehi et al.[29] report an exponential decay of the gas density away from an orifice from a simulation of gas jets for different pressure differences between the inside of the nozzle and the chamber. Experimental measurements of the pressure gradient away from the nozzle by Patel et al.[30] reveal a continuous pressure decrease away from the nozzle for a distance of about 20 orifice diameters (in their experiment about 20 mm for a 0.8 mm orifice diameter), which would correspond to a continuous pressure decrease away from the orifice of about 400 µm for a nominal 20 µm orifice diameter. From comparisons with these results, we suspect a monotonic decrease in gas density and pressure across the microplasma gap in our experimental setup.

However, if the gap distance is reduced by bringing the sample close to the orifice (here about 120 µm), an increase in SE signal is visible on the sample surface as well (Figure 1b, dashed arrow). The increased SE signal at the sample indicates an increased gas density at the sample surface. From these observations, it becomes clear that the gas density profile in the gap depends, among other parameters, also on the gap distance. This non-uniform gas pressure impedes predictions and comparison with conventional plasma reactors with a constant pressure between the electrodes. As a beneficial side aspect, the visible gas spot on the sample surface can be used to predict the plasma-spot region. This can be seen by comparing the images before and after plasma operation in Figure 1b,c, respectively, where the pit due to plasma sputtering forms in the region predicted in Figure 1b.

2.1.2. Voltage–Current Characteristics of the Plasma

Next, the voltage-current characteristics (i.e., the dependence of discharge voltage V_D and discharge current I_D) of a N_2 microplasma were investigated for three gap distances (75, 100, and 125 µm) and three gas flow rates (2.5, 5.0, and 7.5 sccm). Nitrogen was chosen over Ar because it resulted in lower chamber pressures for the same gas flow rate, allowing for higher gas flow rates (up to 8 sccm) into the high-vacuum microscope chamber. The pumping speed of different gases is discussed in more detail in the supplementary information. For each gas-flow/gap-distance pair, two measurements were taken for repeatability (here denoted in the brackets in the figure legends). **Figure 2**a–c shows the values sorted with decreasing gap distance from left to right. The same axis limits were used for easier comparison.

In general, a positive slope is visible for all curves, indicative of a so-called abnormal glow discharge plasma.[6] This was also observed by Matra et al.,[22] but not in all of their measurements. After this initial positive increase of discharge current with discharge voltage, nearly all curves show a maximum current followed by a current decrease (cf. arrows in Figure 2b,c). The last aspect is a measurement artifact, probably caused by rapid sputtering of the electrode, and should not be interpreted as an actual voltage-current characteristic of the microplasma. This artifact is discussed in more detail in the supplementary information (Figure S1, Supporting Information).

Next, the ordinate intercepts of the curves in Figure 2 are discussed. These points correspond to the lowest discharge voltage at which a plasma discharge can be sustained. Note that this is not equal to the breakdown voltage, as the voltage required to initiate a breakdown is often (significantly) higher than the voltage required to sustain one.[5] The actual breakdown voltages were not measured since our setup does not produce the necessary uniform gas pressure for a given gap distance for a controlled measurement.[31] Figure 2a–c shows a decreasing minimum discharge voltage for increasing gas flow rates for the same gap distance. Since an increase in gas flow rate for a constant

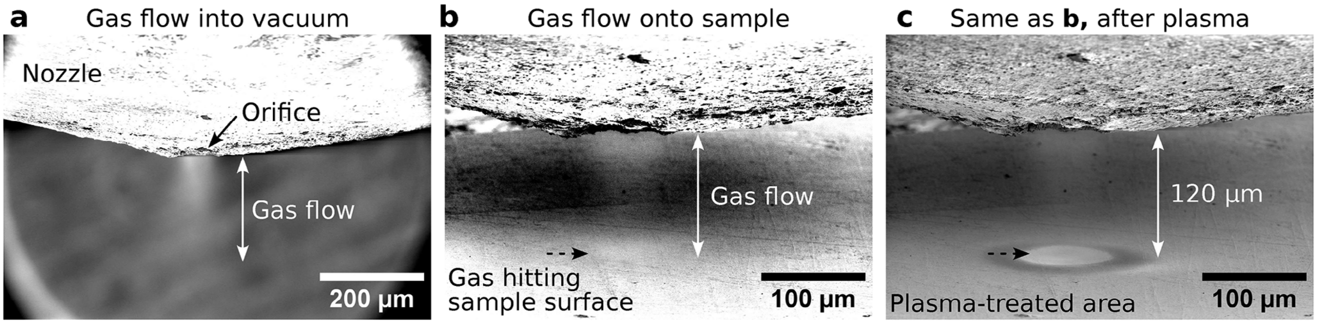

Figure 1. Investigation of the gas density profile in the plasma gap. a) SE-SEM image of the gas flow into vacuum acquired with a primary electron energy of 2 keV. b) A spot with a slightly increased SE signal is visible on the sample surface (marked with a dashed arrow) when a sample is brought into proximity, probably due to an increased gas density when the gas jet hits the sample surface. c) After plasma treatment, the bright spot coincides with the plasma-treated region, indicating that the gas spot in (b) can be used for aiming the microplasma at the desired region of interest.

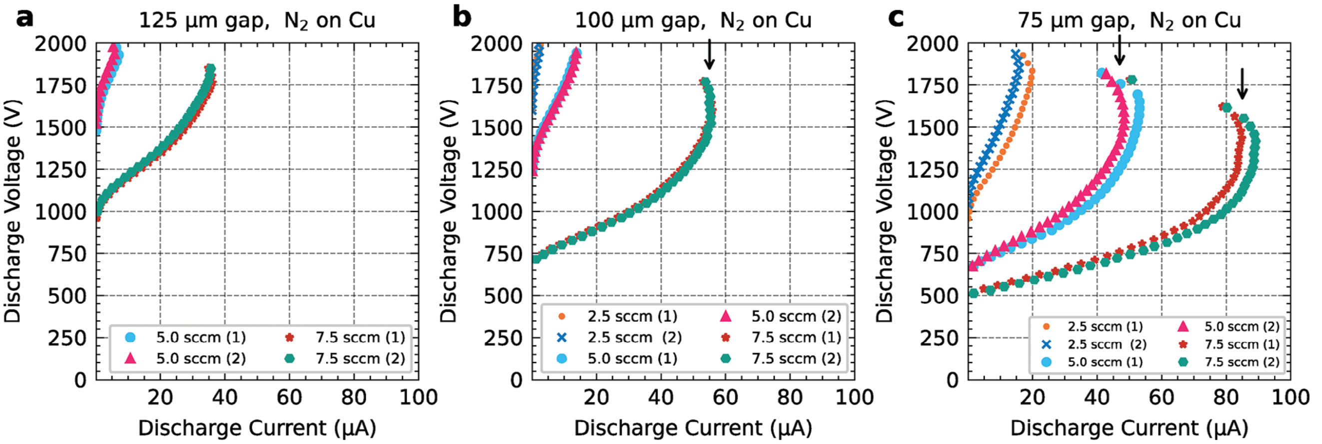

Figure 2. Voltage–current characteristics of a N_2 microplasma for different gas flow rates and gap distances. All axis limits are equal for easier comparison. The data is shown for decreasing gap distance from left to right. Two measurements were performed for each gas flow rate and gap distance. No discharge was observed for 125 µm/2.5 sccm. Slight deviations between these measurements are mainly caused by uncertainties in gap distance. The apparent drop in current for higher voltages (marked with arrows in (b) and (c)) is a measurement artifact caused by sample-surface sputtering. In general, larger discharge currents are observed for higher gas flow rates and smaller gap distances. A positive slope for all curves indicates a so-called abnormal glow discharge behavior.

gap distance is assumed to result in an increasing gas density, this decreasing minimum discharge voltage offers an interesting insight into the plasma discharge. As described by the Paschen curve for simple parallel-plate and uniform-pressure DC plasma systems, an increased pressure heavily affects the discharge properties (see also Figure S2, Supporting Information).

On the one hand, if the gas density is higher than the optimum (i.e., the point with the lowest minimum discharge voltage, similar to the minimum in the Paschen curve), the electrons undergo many collisions, which limit their possibility to gain enough energy to ionize a molecule. This ionization is required to create an avalanche effect, which is needed to sustain a discharge. In this case, a higher voltage is required to sustain the discharge to ensure the electrons can gain sufficient energy to cause subsequent ionization.

On the other hand, if the gas density is lower than the optimum, the electrons can easily gain sufficient energy, but they may not collide frequently enough to cause the further ionization required to sustain the discharge. Then, again, a higher voltage is required to ensure that the collisions will cause ionization. As the minimum voltage required to sustain a discharge decreases with increasing gas density, it is implied that the gas density is lower than the optimal case overall. This is analogous to being on the left side of the minimum in the Paschen curve. It should be noted, though, that given the strong pressure gradient in this setup, the discharge mechanisms are not as straightforward as they are assumed by the Paschen curve, so a direct comparison is difficult. This behavior of the minimum discharge voltage implies that the plasma could be categorized as a so-called obstructed abnormal glow discharge.[5,6]

When comparing the curves for the same gas flow rate and different gap distances in Figure 2a–c, both the gas density and the gap distance are varied since the former is affected by the latter. Assuming that the gas density at a constant gas flow rate increases for a decreasing gap distance, the changes in minimum discharge voltage in Figure 2a–c indicate that the gas density is increasing non-linearly (in contrast to a linearly decreasing distance) and more substantial than the gap distance.

An additional complication affecting the interpretation of the data is the setup geometry. The shown setup with a rounded nozzle with an orifice as one electrode and a possibly textured sample surface as another electrode is different from earlier publications studying various electrode geometries.[31–34] Microplasmas are especially sensitive to surface effects due to the small spatial scale in the sub-mm range, as the electric field can be strongly altered by small morphological changes in the electrode surfaces.[34] In addition, due to the high-pressure gradient, it is impossible to accurately control the pressure in the discharge gap using this setup.

2.1.3. Plasma Generation and Stability in an SEM

The plasma-in-SEM setup enables studying the interplay between the electron beam of the SEM and the plasma. Different aspects of this interaction are discussed in the following.

First, an electron beam can be used to ignite the plasma at lower voltages than required for the self-ignition when reaching the breakdown voltage[13] (**Figure 3a**). For example, in one case a plasma discharge could not be achieved, even when applying a maximum source voltage $V_S = 2$ kV to the nozzle without an electron beam. However, scanning with the electron beam caused a plasma discharge already at $V_S = 920$ V for the same gap distance and gas flow rate. This can be explained by the generation of SEs, backscattered electrons (BSEs), and X-rays upon the interaction of the electron beam with the sample, which then triggers the plasma ignition. Notably, the electron beam ignites the plasma even if it is not directly scanning in the gap region. No changes in plasma discharge current or plasma behavior were observed between the electron beam scanning inside or outside the central plasma-spot region, that is, the plasma was unaffected by the exact electron-beam position during discharge. This shows that the

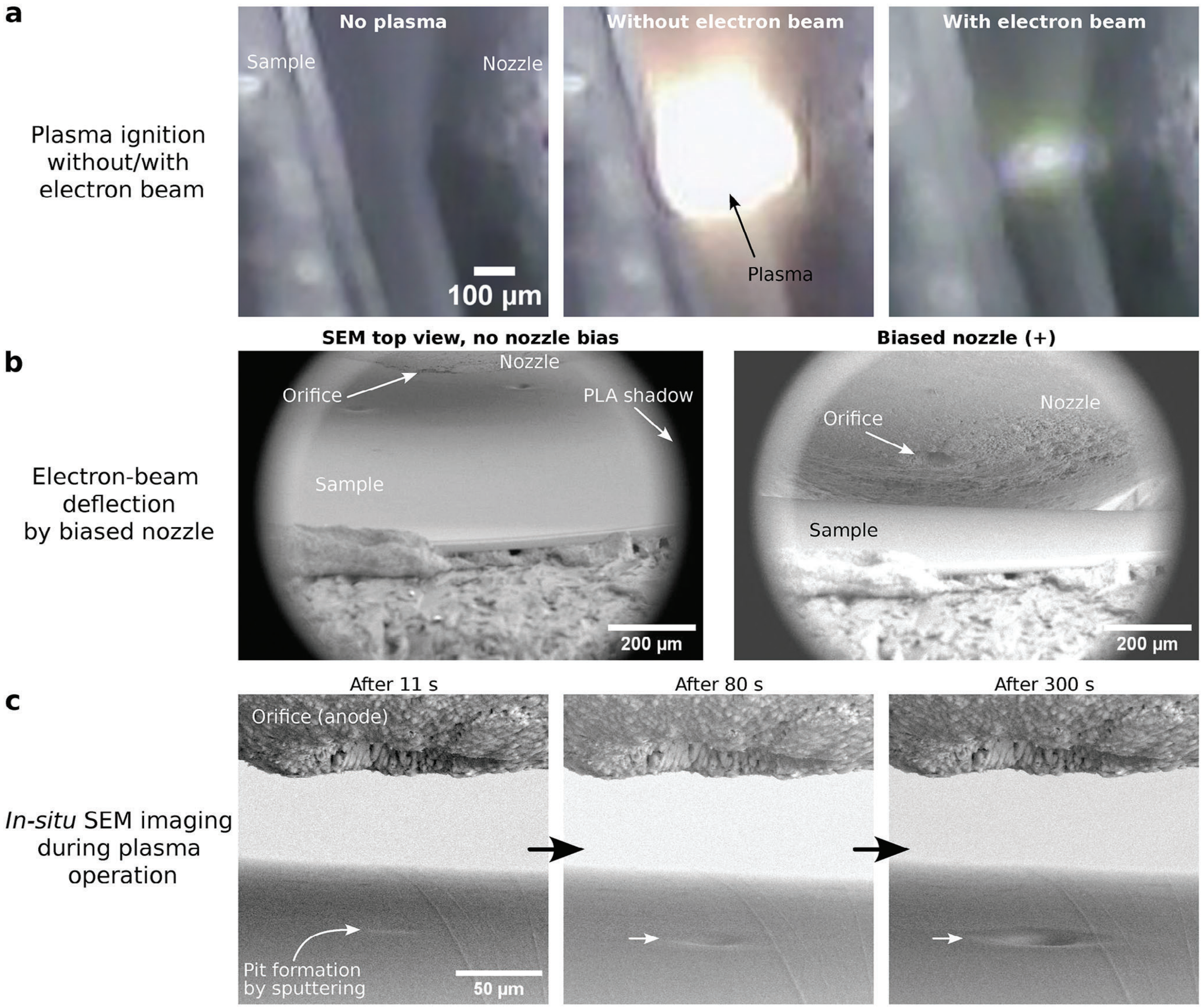

Figure 3. Aspects of microplasma operation in a scanning electron microscope. a) Webcam images of plasma operation. The electron beam can be used to ignite the plasma at a lower applied source voltage to generate a less intense plasma (right) compared to self-ignition by reaching the breakdown voltage (middle). The shown plasma images correspond to the plasma conditions right after plasma ignition. b) Top-view SE-SEM images (10 keV) of the nozzle and sample (left) without and (right) with applied voltage on the nozzle ($V_S = 920$ V). In this example, the electrons are attracted to the positive potential on the nozzle, which enables imaging of the orifice area. c) True in situ SE-SEM imaging during plasma operation is possible and shows the formation of a pit in the sample due to sputtering.

generated signals (SEs, BSEs, and X-rays) serve as the ionization source for the plasma. However, small effects may still be present and could be below the detection limit of our setup. For example, sample sputtering during plasma operation led to continuous changes in discharge current which might overshadow small changes in plasma behavior when the electron beam is scanning the plasma cloud.

A webcam video comparing plasma ignition by (i) reaching breakdown voltage (the conventional way) or (ii) using the electron beam is found in the supplementary information (Video S1, Supporting Information). In this video, the SEM-triggered plasma shows a less intense plasma cloud than the self-ignited plasma. Therefore, the electron beam can be advantageously employed to ignite a less intense plasma at lower voltages (cf. the middle and right images in Figure 3a). In addition, for conditions where a plasma is not self-sustainable, that is, with a large gap distance and/or low gas flow rate, a plasma discharge was observed that was only active during active electron-beam scanning (see Figure S3, Supporting Information).

Second, applying an electric potential to the nozzle will create an electric field that deflects the incoming electron beam, for example, toward the positive potential on the nozzle (Figure 3b). The deflection depends on the electron energy (less deflection for higher keV) and probably also on the extent of the exposed metal part of the steel nozzle. In our setup, insulating tape was used to cover most of the steel nozzle, excluding the tip (see black tape in Figure 9). The deflection may be minimized by: i) shielding the open metallic surface of the nozzle tip and ii) using a higher primary electron energy. However, the deflection can also be used advantageously. For example, the deflection can be strong enough so that the SE-SEM image is formed from the nozzle-tip surface, for example, at $V_S = 920$ V for a primary beam energy of 10 keV (Figure 3b, right). In this way, the tip region of the nozzle can be imaged with the SEM even though it is aligned parallel to the electron beam, that is, without a direct line of sight. This effect is more pronounced at lower electron energies. A supplementary movie (Video S2, Supporting Information) shows correlative imaging of the webcam and SEM images during a gradual increase in the source voltage V_S and subsequent SEM-induced plasma ignition. The SEM image is increasingly "tilted" toward the nozzle with increasing V_S.

Third, it was observed that in situ SEM imaging during plasma operation is indeed possible, opening up the opportunity for time-resolved studies. In SE-SEM imaging, a working plasma leads to an increase in signal (brightness) using the Everhart–Thornley detector (ETD). For imaging, this effect can be compensated by reducing the ETD bias setting. For a CO_2 plasma, this method proved effective for discharge currents up to about 7 µA, after which the ETD was saturated (i.e., no further reduction in bias was possible), and no SE-SEM imaging was possible. It is remarkable that in situ SE-SEM imaging during plasma operation is feasible, despite several challenges: i) the total electron-beam current used (few nA) is about a thousand times lower than the measured discharge current (few µA), ii) many spurious SEs are likely generated in the plasma region,[5,6] and iii) the positive suction voltage on the ETD of +250 V to attract SEs is comparatively low compared to the nozzle voltage (typically >1 kV). Even though the total electron-beam current is lower than the discharge current, the higher current density of the electron beam j_e compared to the plasma-current density may locally generate enough SEs to give a sufficient signal for SE-SEM imaging. For example, a 1 nA electron probe with a diameter of 5 nm results in $j_e \approx 5000$ A cm^{-2}, which is significantly larger than the plasma-current densities used in this work, which are in the order of 1 A cm^{-2}. Three SE-SEM images taken during continuous microplasma operation are shown in Figure 3c. The plasma duration increases from left to right, leading to increasing pit diameter and depth due to surface sputtering. The most notable distortion in the SE-SEM image is caused by the applied nozzle voltage, resulting in an electron-beam deflection (Figure 3b).

Similarly, BSE-SEM imaging was tested by negatively biasing the ETD with −150 V to suppress (mainly) SEs from the image signal. In contrast to SE-SEM imaging, the BSE-SEM image brightness is not affected by the discharge current during plasma operation, meaning that BSE-SEM imaging is still possible even when the SE signal becomes saturated at high discharge currents (e.g., >7 µA for CO_2). A video comparing BSE- and SE-SEM imaging is found in the Supporting Information (Video S3, Supporting Information). Since the ETD covers only a relatively small solid angle, it is inefficient for BSE detection. This results in a lower signal yield than for SE-SEM imaging. However, the low BSE signal may be increased by using a more efficient and low-vacuum compatible BSE detector,[35,36] but this was not tested in this work. Since both SE- and BSE-SEM imaging are possible and similar to conventional SEM imaging, the signals can be chosen depending on the experiment, or both signals can be collected with two different detectors. This enables more surface-sensitive imaging with SEs and Z-dependent imaging with BSEs.[21] Overall, these results demonstrate that in-situ SEM imaging during plasma treatment is possible, which opens the possibility for time-resolved in situ studies. The quality of SEM imaging during plasma treatment is hampered by beam deflection and additional SE signals from the plasma, but these aspects may be improved. For cases where the highest spatial resolution of the SEM is required, intermittent switching between SEM imaging and plasma treatment can alternatively be applied so that SEM imaging is not deteriorated by the plasma cloud and the applied voltage on the electrodes.

An application-relevant observation from the demonstrated setup is the absence of undesired high-current and high-frequency arc discharges, which were reported by Matra et al.[22] as a self-pulsating plasma mode. Instead, we observed stable DC glow discharges with discharge currents ranging from about 0.1 to 175 µA, which can be controlled by adjusting V_S. This corresponds to current densities ranging from 5 mA cm^{-2} to 9 A cm^{-2} for an assumed plasma-spot diameter of 50 µm. The latter can vary depending on the gap distance. We did not investigate higher currents than 175 µA since the 30 µm thick Cu target is sputtered away in a few (ten) seconds at the plasma spot. Conversely, the plasma could not be sustained below the lower limit of about 0.1 µA.

The absence of arcing may be explained by the lower chamber pressure in our used SEM (about 2×10^{-2} Pa) compared to the reported values "below" 1 Pa.[22] Notably, a self-pulsing plasma was observed for the shown setup when powering it in ambient air during prototyping. The high-frequency arcing in this self-pulsing mode (a few 10 kHz) causes significant electromagnetic interference to surrounding electronic devices, including the SEM. In addition, powering the setup in the low-vacuum mode of the SEM at a chamber pressure of 40 Pa leads to undesired discharges in the SEM chamber, similarly as observed by Pardinas.[15] This restricts the plasma operation to the high-vacuum mode (below 3.3×10^{-2} Pa for the used SEM). Here, only occasional arcs during plasma operation were observed when non-flat samples with surface protrusions were used. It may be possible to fully mitigate the self-pulsing plasma mode with an optimal choice of electronic components in the circuit. Still, in our case, the reduced chamber pressure (about 2×10^{-2} Pa) is the most likely reason for a stable DC plasma operation compared to Matra et al.[22] The reduction of arcing in our setup is an important step toward better control and optimization of the plasma conditions for plasma-in-SEM studies.

2.2. Microplasma Applications

2.2.1. Sputtering and Cone Formation

Sputtering is the process of removing atoms of the target material by impinging ions. Sample material was removed by this process in all experiments, where the sample was used as the cathode. The positively charged ions are accelerated toward the cathode and cause sputtering, as is common in glow discharges. This results in changes in surface morphology in the plasma-spot regions, with diameters ranging from about 50 to 150 µm (depending on the gap distance, pressure, discharge voltage/current,

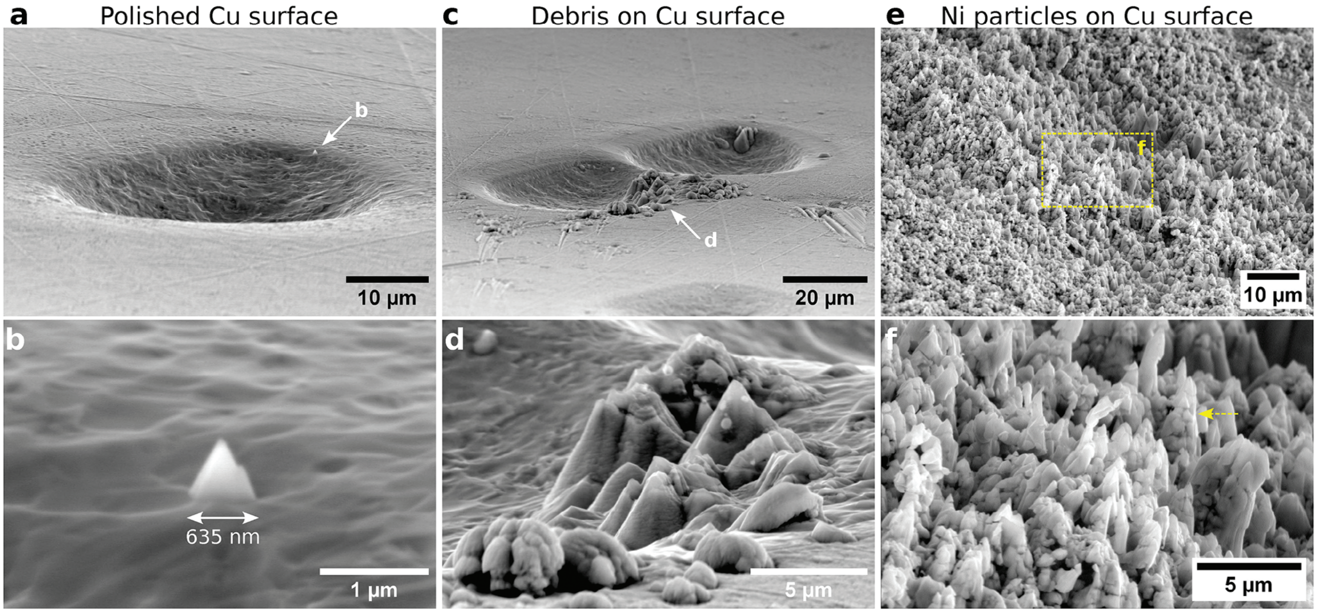

Figure 4. Cone formation after Ar$^+$-ion sputtering for different concentrations of surface particles. The lower row shows higher magnification SEM images of the upper row. a) Cone formation is not visible in the shown region of a polished Cu surface. b) A small cone is visible on the edge, probably due to a small contaminating particle on the sample surface. c, d) Debris on the Cu surface forms cones under plasma treatment. e) Ni particles deposited on a Cu substrate show clear cone formation in the plasma-treated region. In the early stages of sputtering, the Ni particles locally agglomerate to form a cone (see the example in (f) marked with a dashed arrow).

and plasma duration). In the following, results for sputtering on: i) a polished or ii) a Ni nanoparticle-covered Cu surface are shown.

The formation of a pit under CO_2 and Ar-containing plasma was observed for a polished Cu surface. An example is shown in **Figure 4**a, which was created with Ar plasma. Experimentally, this pit formed after 1.2 keV Ar$^+$ exposure with a discharge current of about 15 µA (current density of 1.2 A cm^{-2} for a plasma-spot pit diameter of 40 µm) for about 10 s. The rapid pit formation is indicative of the high sputter rates of the setup. The pit surfaces are rougher than the original polished surface. A comparably small conical structure is visible at the edge of the pit, which is magnified in Figure 4b. This may have been an impurity or other contamination present in or on the Cu surface, which deformed to the shown conical structure during sputtering. Its bright appearance in the SE-SEM images may be explained by the penetration depth of primary electrons, here at an energy of 15 keV. For relatively thin structures such as the impurity shown in Figure 4b, SEs are emitted not only on the entrance surface of the beam but also on the exit surface of the cone (and also the sample material behind the cone). The additional SE emission from the exit surface (relative to the incoming electron-beam direction) leads to higher SE-SEM image intensity for thinner sample regions.

Cone formation is observed for random debris (Figure 4c,d) or full coverage with Ni nanoparticles (Figure 4e,f). For the latter, the nanoparticles seem first to cluster together (see region marked with an arrow in Figure 4f) and then tend toward a conical shape during prolonged sputtering. The latter aspect was studied in more detail by monitoring the same area after a certain plasma duration with SEM imaging (**Figure 5**). Between each plasma treatment, the sample area was moved onto the optical axis of the SEM to allow for high-magnification imaging. A few exemplary areas are annotated with arrowheads, which are discussed in the following.

Region (1) shows the shape evolution of Ni particles under Ar plasma. Between 0 and 30 s, the shape gradually changes from round nanoparticles (Figure 5a) toward a conical shape (Figure 5d). After reaching the final conical shape, the cone is milled away during further sputtering (cf. region (1) for Figure 5d,e). Similarly, region (3) shows the removal of smaller cones between 30 and 60 s of sputtering (cf. region (3) for Figure 5d,e). For region (2), a few Ni nanoparticles agglomerate between 10 and 20 s. It is unclear from the images if these particular particles result from the present particles in the shown region or were redeposited from remote sample areas. Further plasma exposure leads to a merging of the individual nanoparticles and the formation of a larger cone with smooth surfaces (cf. region (2) for Figure 5d,e). Overall, after 60 s, the underlying Cu surface is partly exposed (Figure 5e).

The observed formation of cones is a commonly observed modification of metal surfaces under ion bombardment.[37–39] The cone shape is commonly thought of as a combined result of varying sputter yield depending on the: i) ion-incidence angle and ii) material. The sputter yield typically increases with increasing ion-incidence angle up until a maximum value Θ_m, and then decreases rapidly toward grazing incidence (i.e., the ion direction being parallel to the sample surface).[38] This results in a cone shape of impurities and surface particles before complete removal by sputtering. The seeds for the cones can be intrinsic elemental impurities on an otherwise flat surface or particles on the surface with a lower sputter yield. The latter correlates with the melting temperature of a material. Wehner[39] has tested

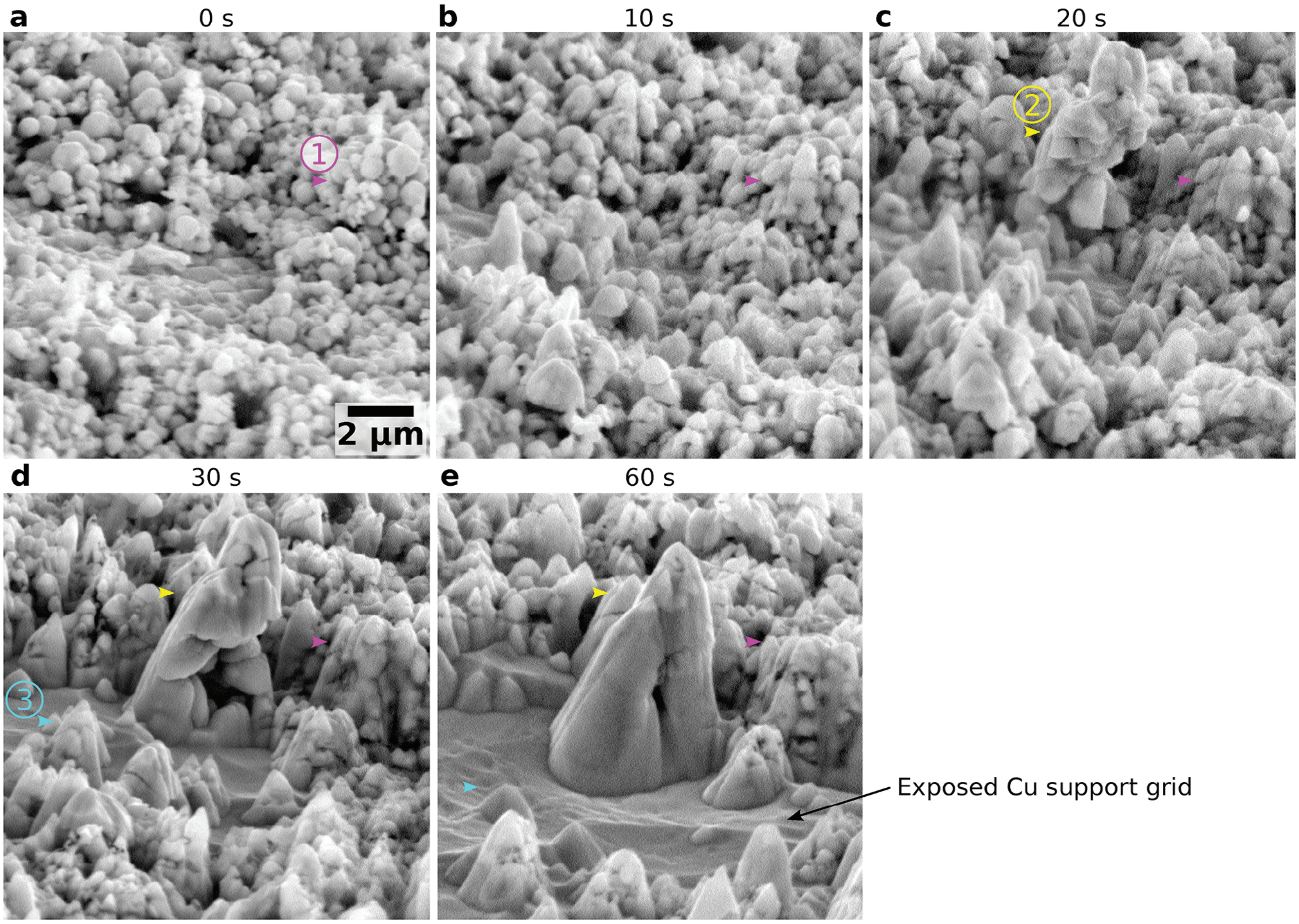

Figure 5. Quasi in situ observation of Ni nanoparticle agglomeration and subsequent cone formation during Ar$^+$-ion sputtering (5 µA, 1.32 keV) for the given duration shown above the SE-SEM images. The latter were taken with a large-field detector (LFD) in the low-vacuum mode (40 Pa) after each plasma operation in high-vacuum mode. A few interesting regions are marked with arrows. Region (1) shows a gradual change from (a) a round particle morphology to an increasing distortion toward a conical shape. After reaching the latter in (d), the cone is then starting to be removed by sputtering, as visible in (e). Region (2) shows the sudden agglomeration of a few nanoparticles in (c). A larger cone is forming from this agglomeration (d,e). Region (3) exemplifies that, after initial formation, the cones are sputtered away under further Ar$^+$-ion bombardment (d,e).

numerous surface/seed combinations of metals with different melting temperatures and found that cone formation requires seed materials with higher melting temperatures than the surface material. This is the case for Ni particles (T_{melt} = 1728 K) on a Cu substrate (T_{melt} = 1358 K) as observed in Figure 5. Note that the used nanoparticles are large enough (around 100 nm) so that a reduction in melting points is assumed to be negligible.[40,41]

A mean apex angle of $\Theta = (61.4 \pm 11.1)^\circ$ (the error being the standard deviation) was measured for 40 cones. According to Stewart and Thompson,[42] Θ is related to the ion-incidence angle for maximum sputter yield Θ_m, as $\Theta_m = (180^\circ - \Theta)/2 = (59.3 \pm 5.6)^\circ$. The experimental value Θ_m is in good agreement with the maximum $\Theta_{m,\,\text{sim}} \approx 65^\circ$ of a simulation of the angle dependence of the sputter yield of Ar on Ni using SRIM (Figure S4, Supporting Information). The differences between measured and simulated values can be explained by: i) limited statistics based on only 40 measured cones, ii) systematic errors in the angle measurement from SEM images, and iii) uncertainties in the simulation.[43]

2.2.2. Local Oxidation

Plasma finds applications in both the oxidation and reduction of materials.[44,45] Here, we investigate the possibilities of local plasma-induced sample oxidation in the SEM. As a first example, a polished Cu surface was exposed to a CO_2 plasma (**Figure 6**). The gap distance was ≈130 µm (Figure 6a). In Figure 6a, a sputtered hole from a previous experiment is visible in the top right corner, and the nozzle is visible in the bottom right corner. The applied source voltage was V_S = 2 kV and discharge currents between 70 and 120 µA were measured. After 10 s of plasma operation, Figure 6b, a pit starts forming with a diameter of about 70 µm. Chemical analysis by EDS shows increased Cu and decreased O signals in the pit region, indicating a removal of the native Cu oxide by sputtering. This exposes the underlying Cu metal, leading to a higher Cu Lα signal. After 50 s, the pit is widened to about 100 µm diameter (Figure 6c). The sputtered pit area still shows a higher Cu signal than the unaffected Cu surface around it, similar to Figure 6b. The reduction in Cu Lα signal in the top part of the Cu elemental map in Figure 6c results from

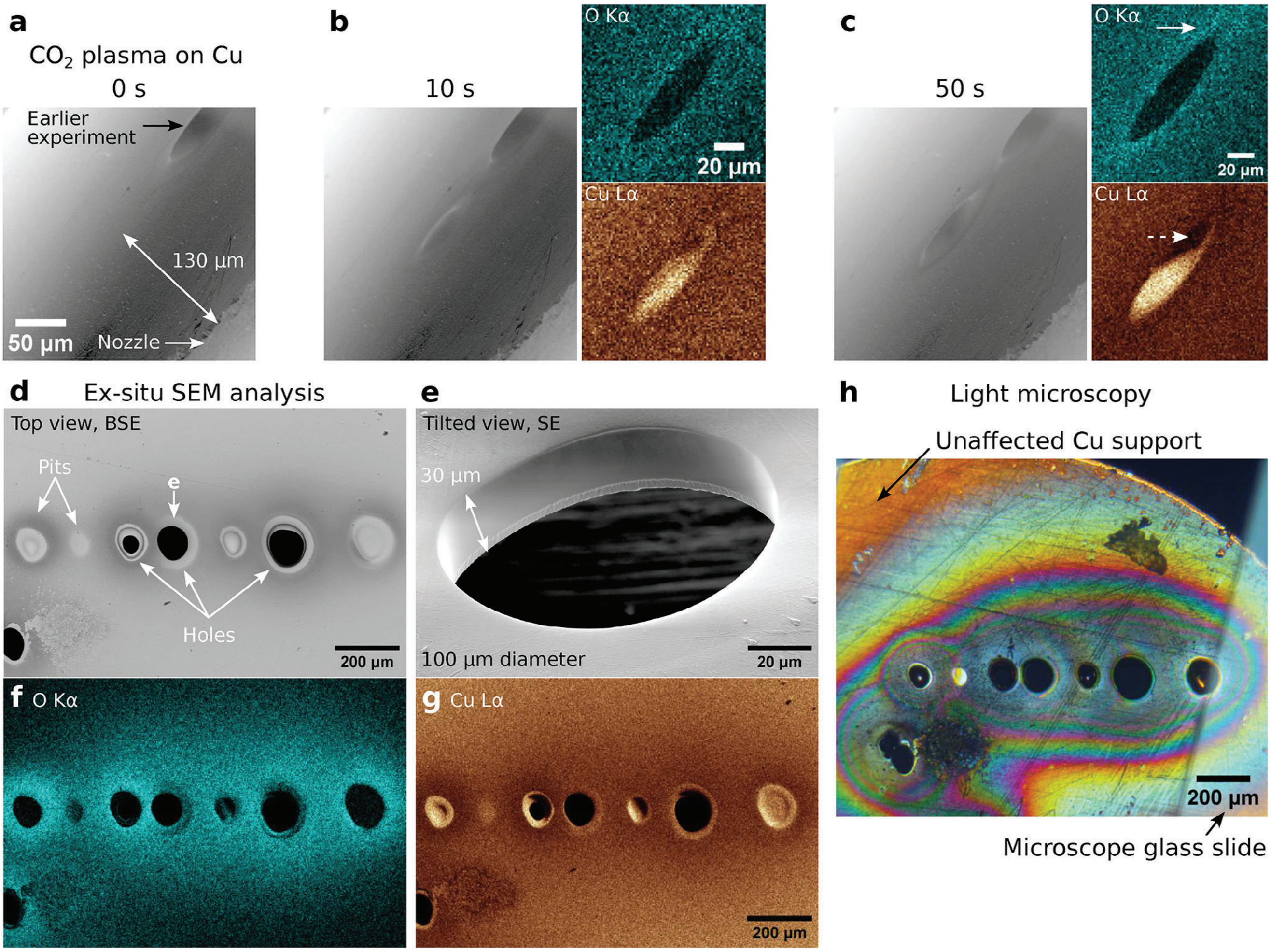

Figure 6. Sputtering and oxidation of a polished Cu surface under CO_2 plasma. a) SE-SEM image showing the sample surface opposite to the nozzle with a 130 µm gap. The hole in the top-right corner is from an earlier experiment. b,c) Images and O/Cu elemental maps after 10 and 50 s plasma treatment. A pit forms due to sputtering. A higher Cu signal in the pit indicates the removal of the native oxide in the plasma spot. c) Enhanced O signal is visible at the pit's edge (marked with a solid arrow). The depletion of Cu signal is due to the shadowing of the X-ray signal toward the detector. d) Top-view BSE-SEM image of various pits and holes in the Cu foil after plasma treatment. e) Side-view SE-SEM image of a hole showing vertical side walls. f,g) The elemental maps reveal enhanced oxidation around the plasma spots and higher Cu signal in the pits similar to (b,c). h) Light-microscopy image showing interference effects in the oxidized regions around the plasma spots.

shadowing of the generated Cu Lα signal X-rays from the inside of the pit toward the EDS detector. An increase in O Kα signal is visible at the pit's edge (Figure 6c). This observation indicates the oxidation of Cu in this region. The O signal increases under prolonged CO_2-plasma exposure (not shown here), which we attribute to the continuous growth of this Cu-oxide layer.

The sample was investigated again in the SEM and using light microscopy after the in-situ experiments (Figure 6d–h). The top-view BSE-SEM image acquired at 20 keV shows different experimental sites of local CO_2 plasma treatment (Figure 6d). The black areas show regions where the total thickness (about 30 µm) of the Cu support was sputtered away, leaving holes behind. One of the holes is also displayed in the SE-SEM image in Figure 6e. The tilted view reveals the high aspect ratio of the sputtering process, resulting in vertical sidewalls. The elemental map of O shows an increased O signal around the plasma spots, similar to Figure 6c, which is decreasing in radial direction away from the spots. For the pits, the removal of the native oxide layer of Cu leads to an increased Cu Lα signal. The increased O concentration around the holes reduces the effective atomic number relative to metallic Cu. This results in a reduced BSE intensity in Figure 6d in the oxidized regions due to the BSE signal's atomic number Z dependence.[21] Interestingly, the oxidation of the Cu surface reaches a few hundred µm away from the initial plasma spots. This phenomenon is more clearly visible in the light-microscopy image (Figure 6h), which shows interference effects related to the gradually changing thickness of the grown Cu-oxide film (Newton rings). In the top left corner of the image, there is an unaffected (i.e., without plasma-induced oxidation) area of the sample (marked with an arrow in Figure 6h). Overall, the polished Cu surface is sputtered away under CO_2 plasma. A local CO_2 plasma causes oxidation around the plasma spot, probably forming a Cu-oxide film with decreasing thickness away from the plasma spot. This oxidation is most likely caused by oxygen species (such as

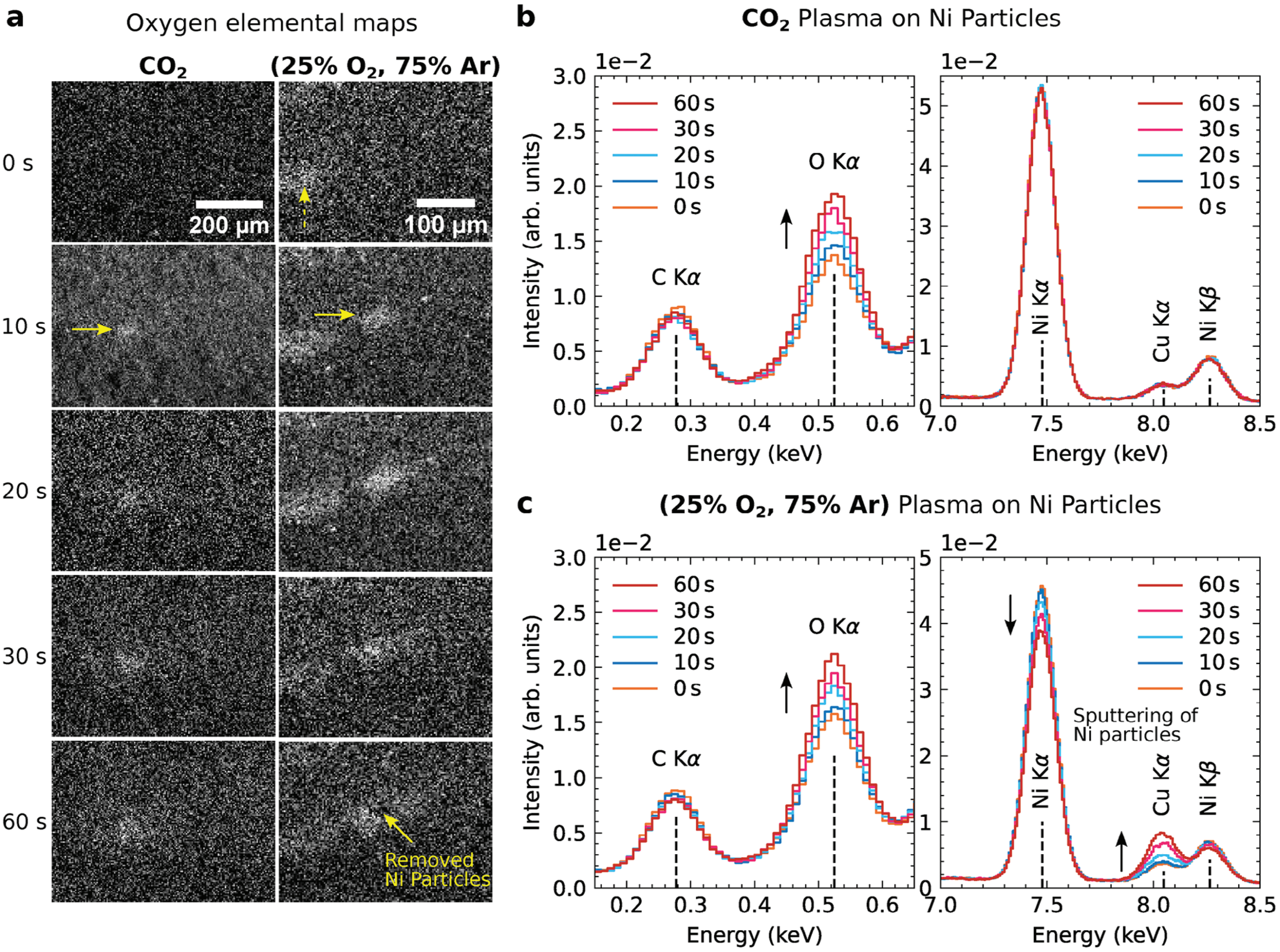

Figure 7. Local oxidation of Ni particles under CO_2 and O_2/Ar plasma treatment. a) Elemental maps showing the O Kα intensity for increasing plasma duration between 0 and 60 s (top to bottom) for CO_2 plasma (left column) and O_2/Ar plasma (right column) for similar discharge current (about 5 µA) and gap distance (about 250 µm). A spot of local oxidation is visible after 10 s (marked with horizontal arrows). The O-rich spot at 0 s for O_2/Ar is from a previous experiment (dashed vertical arrow). b,c) Comparison of extracted EDS signals in selected energy regions for the O (left), and Ni and Cu energy regions (right). The increase in O signal for increasing plasma duration is visible. For O_2/Ar plasma, sputtering of Ni particles and subsequent exposition of the underlying Cu support reduces the Ni Kα signal and increases the Cu Kα signal (c). This effect is absent in (b), indicating a significantly reduced sputter yield for CO_2 plasma. For comparison, the EDS spectra in (b) and (c) were normalized to the integrated signals in the energy intervals [2 keV, 5 keV] and [10 keV, 14 keV] containing only bremsstrahlung background signal.

atomic or ionized O) generated in the plasma. These species can be transported out of the plasma (so-called afterglow) by the gas flow, explaining why the oxidation of the Cu is observed away from the plasma spot as well. However, it is noteworthy that the sample temperature was not measured in our experiments. Local sample heating with CO_2 flow may also contribute to Cu oxidation.

Next, similar experiments with CO_2 plasma on Ni nanoparticles were performed (**Figure** 7a, left column). The Ni particles were deposited on a Cu support film and formed a layer with a (varying) thickness of a few µm (Figure 4e). The gap distance was 250 µm, and the discharge current was 5 µA. Local oxidation was observed *inside* the plasma spot, as marked by the arrow in the elemental map acquired after 10 s plasma exposure. The O signal increases with increasing plasma duration from 0 to 60 s. This aspect is not as evident in the noisy elemental maps but more clearly visible in the summed-up and normalized EDS spectra (see Figure S5, Supporting Information, for details) from the plasma-spot region as an increasing O Kα peak (Figure 7b, left). This observation is different from the oxidation *outside* the plasma spots observed for a flat Cu sample (Figure 6). This may be caused by a more pronounced sputtering of Cu compared to Ni, where any oxidized Cu in the central plasma spot is directly removed by ion bombardment. In addition, the ion dose applied to the Ni nanoparticles (Figure 7, 5 µA) was lower than for bare Cu (Figure 6, about 70 to 120 µA), resulting in more sputtering for the latter. In addition to the reduced sputtering effects, many other aspects can affect the oxidation rate and it is not fully clear from our experiments what exactly causes the observed differences between flat Cu and Ni nanoparticles. One aspect is the differences in surface morphology (flat Cu surface vs rounded Ni nanoparticles) affecting the oxidation rates.[46] In addition, considering a possible heating of the sample during plasma, Cu typically oxidizes at lower temperatures than Ni,[46] even though nanoparticles oxidize at lower temperatures than a bulk material.[47,48] For the lower plasma current of 5 µA and the Ni nanoparticles, the local sample heating for oxidation might be only high enough in the central plasma-spot area. In contrast, for Cu and 50 to 70 µA discharge current, the stronger heating (and maybe a better heat transfer for flat Cu bulk compared to Ni nanoparticles) may result in sufficient sample temperature for oxidation outside of the central plasma spot. Furthermore, the amount of reactive species (e.g., atomic O) formed inside the plasma will also be higher in the higher-current experiments, which may also contribute to the more extensive oxidation. Plasma-induced oxidation is another aspect, which is likely different for a flat Cu surface[49,50] and Ni nanoparticles. In plasma-based oxidation, many parameters affect the oxidation rate (pressure, ion energy, incident angle, plasma temperature, ionization degree, exposed facets,...), further complicating a detailed comparison between the observed differences in Cu and Ni oxidation. Overall, a clear explanation is not possible based on our experimental results.

Besides oxidation, the sputtering during CO_2 plasma changed the morphology of the Ni particles inside the plasma spot from round shapes toward conical shapes, as discussed earlier (Figure 4). Overall, the EDS signals for Ni and Cu (from the underlying substrate) are nearly unchanged for CO_2 plasma for this ion dose (Figure 7b, right).

Besides using CO_2, oxidation and sputtering of Ni nanoparticles were also studied for a 25% O_2–75% Ar gas mixture (denoted as Ar/O_2 in the following). The plasma parameters were kept the same as for CO_2 (gap distance of 250 µm and an approximate discharge current of 5 µA). The oxidation of the Ni particles by Ar/O_2 plasma is similar to CO_2 plasma; the oxidation is localized to the plasma region (Figure 7a, right column), and the oxidation gradually increases with plasma duration (see O Kα signal in Figure 7c, left). It is noteworthy, that the oxygen-rich spot at 0 s in Figure 7a for Ar/O_2 (marked with a dashed arrow) results from a previous experiment. Overall, the sputter rate of Ni particles for Ar/O_2 plasma is higher than for CO_2. The enhanced sputter yield for Ar/O_2 plasma is evident from the change in Ni and Cu Kα signals in the right plot in Figure 7c, where the Ni/Cu signal decreases/increases due to the continuous removal of Ni particles and subsequent exposure of the underlying Cu support. This aspect is also slightly visible as a reduction of O signal in the central part of the plasma spot in the O elemental map after 60 s (Figure 7a). After the removal of the oxidized Ni particles in this area, the underlying Cu support is not oxidized *inside* the plasma-spot region, leading to the observed O depletion (cf. with O maps in Figure 6f). This observation qualitatively agrees with simulated sputter yields using SRIM (Table S1, Supporting Information), where Ar has higher sputter yields Y than O. However, CO is another typical molecule in CO_2 plasmas[51] that could not be simulated and compared with Ar using SRIM.

Since the sputtering is primarily caused by the bombardment of the grounded sample surface (relative to a positively biased nozzle) with positively charged ions, switching the polarity between the nozzle and the sample can mitigate sputtering. This aspect was verified experimentally by switching the polarity upon using another DC-DC converter (XP Power, CA12N) than the previously used one (XP Power, CA20P). The experiment was then repeated using CO_2 gas and a Cu target. The experimental setup is shown in **Figure** 8a with the EDS acquisition area marked with a dashed line. The polarity between the nozzle and the sample is reversed compared to all other conducted measurements in this work. Comparison of the O elemental maps before and after plasma treatment (Figure 8b) reveals a pronounced oxidation of the surface in a comparatively wide area (about 400 µm diameter), that is, larger than the actual plasma spot. The latter is not clearly visible in the highly tilted view onto the Cu target's surface in Figure 8b, but it is visible in the top-view BSE-SEM image in Figure 8c. This BSE-SEM image was captured during the investigation of the same sample after the plasma experiments using standard SEM imaging parameters. The top-view BSE-SEM image in Figure 8c reveals the plasma spot with a higher image intensity relative to the surrounding dark area related to the oxidized Cu surface. Note that a low primary electron energy of 5 keV was used for BSE imaging to increase surface sensitivity. Based on the increasing BSE-SEM image intensity away from the plasma-spot region toward the unaffected Cu surface, Figure 8c, the O signal seems to gradually decrease away from the central plasma spot. This gradient in O signal is not clearly visible in the O elemental map in Figure 8b due to the highly tilted sample setup, but can be seen in top-view EDS analysis (Figure S7, Supporting Information). The increased BSE-image intensity of the bright plasma spot (Figure 8c) can be explained by mild sputtering in this region by negatively charged ions bombarding the positively charged Cu surface. This removes the oxide layer and reveals metallic Cu, ultimately leading to higher BSE image intensity due to a higher average Z than the surrounding oxidized Cu surface. Even though mild sputtering is present, no large pit or hole is visible in the plasma-spot region (Figure 8d,e) compared to the initially used negative sample polarity (Figure 6d). The plasma spot area has a diameter of about 25 µm (qualitatively marked with a dashed circle in Figure 8d) and shows the formation of small pits with 200 to 300 nm (surface) diameter (Figure 8e). The pit shape was confirmed by additional SEM imaging of the tilted sample for better visibility of the topography (not shown here). Note that the dashed circle only qualitatively shows the plasma-spot region as a guide for the eye. Small pits can also be observed outside of the marked region in Figure 8d but with a lower number density. These pits are likely caused by the sputtering process and may show their initial stage. Overall, the sputtering of the sample surface is highly reduced when the sample surface is positively biased relative to the nozzle.

In the configuration shown in Figure 8a, the mainly positively charged ions are accelerated toward the negatively biased nozzle, resulting in sputtering of the nozzle surface. Indeed, the orifice diameter increased after these experiments and sputtered material was re-deposited inside the orifice (Figure S6, Supporting Information). The sputtered nozzle material is likely also re-deposited onto the opposing sample surface. Since the same nozzle was used throughout all experiments here, previously deposited sample material (mostly Cu) *onto* the nozzle from earlier experiments is now sputtered and re-deposited *from* the nozzle onto the sample (see the schematic in Figure S6j, Supporting Information). In our case, the orifice area was mostly covered with (oxidized) Cu (Figure S6b, Supporting Information) before the

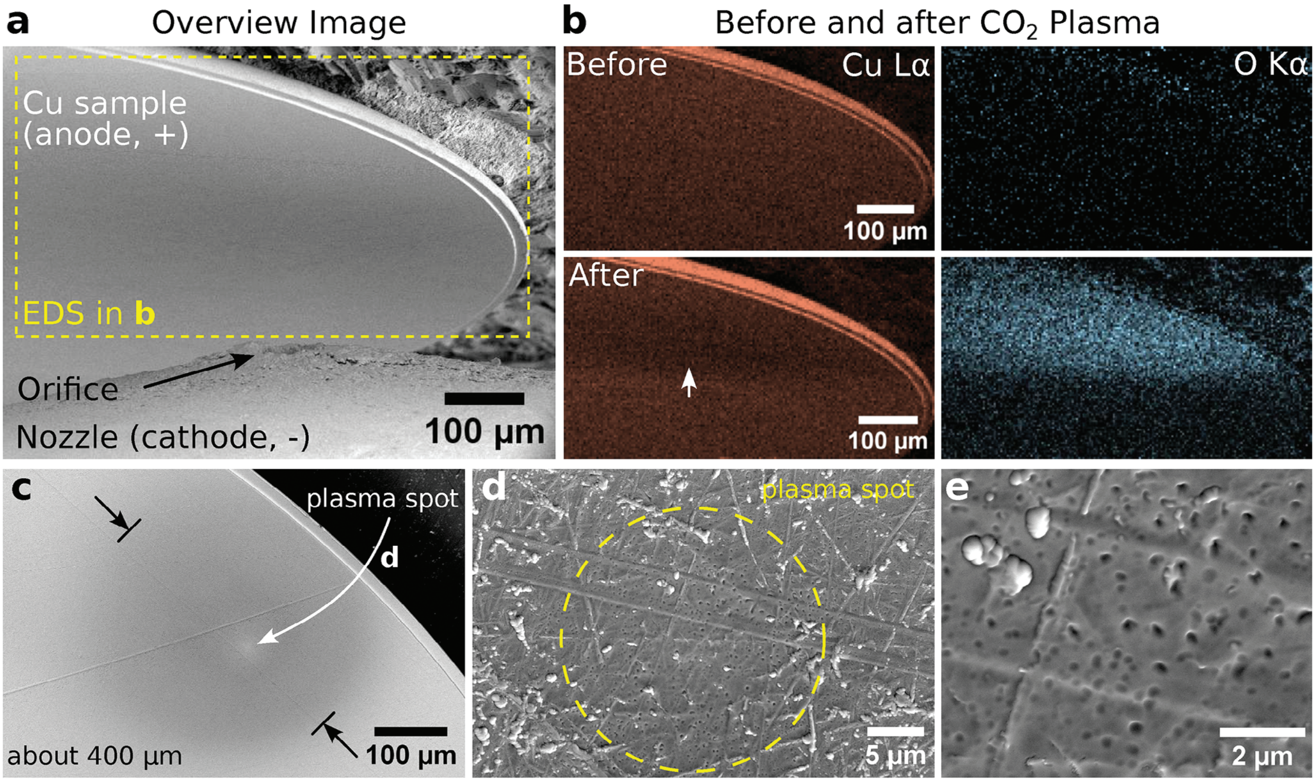

Figure 8. Local oxidation of a polished Cu surface under CO_2 plasma treatment with reversed electrode polarity. a) Overview SEM image of the plasma gap with the EDS region for (b) marked with a dashed rectangle. Note the reversed nozzle/sample polarities. b) Quasi in-situ EDS measurements before (upper row) and after (lower row) CO_2 plasma treatment. The increased O signal is caused by oxidation and re-deposition of oxidized Cu from the nozzle. c) BSE-SEM image (5 keV) of the plasma treated after plasma experiments. d) Higher magnification SE-SEM image of the central plasma spot (qualitatively marked by the dashed circle). e) Pits formed in the central plasma spot, probably caused by ion$^-$ sputtering.

experiments shown in Figure 8, meaning that part of the oxidized region is likely caused by redeposited Cu oxide from the nozzle.

To test this hypothesis, the gas was switched from CO_2 to N_2, and the plasma-treated area showed a N and O signal (see Figure S7, Supporting Information). For a N_2 plasma on a Cu surface, an O signal is unexpected and should not be present without considering the aforementioned re-deposition effects. Our results suggest that part of the O signal in Figure 8b is caused by re-deposited oxidized Cu from the nozzle from previous experiments. Even though this effect is undesirable for pure oxidation with plasma-generated radicals, it may be interesting to study film growth during sputtering. In this explanation, mainly two simultaneous effects lead to the oxidation of the Cu surface. First, reactive O-containing species such as atomic O or O_2 molecules oxidize Cu even far away from the central plasma-spot region since some of these reactive species are long-lived and can thus be transported in the gas flow outside of the plasma volume. The same effect also oxidized the Cu surface for the initial electrode setup (negative sample polarity), where no sputtering (or only mild sputtering) of the nozzle is present (Figure 6). Second, there is the redeposition of previously oxidized material (here mostly Cu oxide) from the nozzle, thus adding O-containing Cu to the sample. Finally, it is also possible that O-containing gas molecules (e.g., water) are present in the SEM chamber during plasma treatment. Such impurity species may also contribute to the observed oxidation during plasma treatment with O-free gases such as N_2.

In summary, oxidation of Ni nanoparticles was observed for CO_2 and Ar/O_2. Oxidation is limited to the central plasma-spot region. For the same ion dose, Ar/O_2 sputtering of Ni nanoparticles is more pronounced than for CO_2. In contrast, oxidation of a flat Cu surface occurs around the central plasma-spot region, which is mostly sputtered rather than oxidized. Sputtering with positively charged ions causes rapid removal of sample material when the nozzle is used as an anode (positive polarity). This results in pits and holes in the central plasma region.

Sputtering of the sample can be strongly reduced by reversing the polarity between the sample and the nozzle, leading to less damage during oxidation. However, sputtering of the nozzle material in this configuration causes damage to the tip of the nozzle and redeposition of this material onto the sample surface. Pure sample oxidation without sputtering or redeposition of material requires other plasma configurations.

2.3. Limitations and Outlook

The current setup presented here demonstrates significant advances compared to the state-of-the-art, including a stable DC discharge, no undesired arcing, and true in situ SEM imaging while the plasma is active. This enables further research regarding plasma-surface interactions, plasma physics, and sputtering, and even provides the future potential to study the plasma constituents with both spatial and time resolution. For example, the investigated processes regarding sputtering, material deposition, and surface oxidation are highly relevant for materials science, nanotechnology, and the semiconductor industry. Despite these advances and the unique possibilities they offer, certain limitations remain, particularly in terms of expanding the scope of potential research areas. For example, fields such as plasma catalysis or biomedical applications of plasma are growing rapidly, increasing the need for more advanced experimental techniques to study, for example, plasma-catalyst or plasma-cell interactions.[52,53] For such research topics, this setup is currently unsuited since sputtering of the sample (or redeposition of material from the nozzle) is undesirable and prevents studying the samples under relevant conditions. In order to study such samples, the sputtering behavior of the plasma should be eliminated. In principle, the current setup could be optimized further to reduce the discharge voltage to decrease the ion energy, lowering the sputtering rates. One potential approach would be to increase the ballast resistor in the system, to limit the current and lower the discharge voltage. Another approach would be to further increase the pressure, as it is expected that the current setup operates below the optimum value. However, increasing the gas flow rate would require an upgrade to the pumping system of the SEM since the current experiments were performed at the limit of the microscope when operating in high-vacuum mode. The pressure could also be increased by decreasing the gap distance, but this would then also increase the probability of unwanted arcing behavior, as was also observed in our experiments.

Depending on the precise desired application or experiment, a fundamentally different plasma type may be required. A number of plasma types could be of interest, each with their own potential applications and limitations, as well as practical drawbacks. We hereby present a non-exhaustive list of plasma types with their advantages, disadvantages, and potential for in-situ SEM applications.

A common plasma discharge is the dielectric barrier discharge (DBD).[5] This alternating current (AC, or pulsed) discharge is characterized by a dielectric layer covering one or both electrodes, limiting the current and thus preventing arc formation. This is a non-thermal plasma which is often used in plasma catalysis and biomedical research. However, DBD plasmas are generally filamentary, where the filaments consist of microdischarges (short duration, high current discharges). These filaments make the plasma treatment of the sample heterogeneous, complicating the analysis, and cause issues with electromagnetic interference. In principle, DBDs can be operated in a uniform mode,[54] but this requires precise tuning of all relevant parameters (including the dielectric material, voltage, frequency, discharge gas, and pressure) further impeding rapid development of such an experimental setup.

An alternative discharge based on the DBD is the so-called surface discharge. This plasma is similar to the DBD, but one of the electrodes is embedded or below the dielectric, whereas the other electrode is placed on the surface of the dielectric. With this, the discharge will be generated at the surface of the dielectric. This plasma still requires AC or pulsed power, but is generally more convenient to operate in a uniform mode.[5]

Another approach could be using a plasma jet. Many geometries exist, either powered by DC, pulsed, or AC power, but they all have in common that the plasma is generated within a device, after which it flows outward, for example, to a sample.[12] The main difference with the setup presented here is that in the current setup, the plasma is generated in the gap between the nozzle and the sample rather than in the nozzle and sent to the sample. A main advantage of such a plasma jet could be the elimination of the sputtering behavior, as charged plasma species are not predominant (or even absent) in the so-called afterglow. Based on this geometry, an electron beam plasma can be generated,[5] of which a variation was previously introduced in an SEM.[14] In such plasmas, a high-energy electron beam is sent through a neutral gas, where the electrons ionize gas molecules. The plasma can then be sent to a sample through a gas flow, or the ions/electrons could be selectively attracted by biasing the sample. An external AC or DC circuit can also be added to further sustain and alter the plasma discharge, depending on the desired properties. Having access to a high-energy electron beam makes an SEM promising to further explore such plasmas.

Note that all AC or pulsed-powered plasmas are very likely to interfere with the true in situ imaging of the SEM since the electron beam will be deflected periodically during scanning, drastically decreasing the image resolution. However, often these limitations can be overcome by employing stroboscopic imaging, where the plasma is momentarily switched off during SEM imaging. Such quasi in-situ experiments can offer a combination of excellent spatial and temporal resolution.

Despite the remaining challenges, this developing technology is exciting, since introducing a microplasma may enable very different experiments and applications. On the one hand, the in situ plasma may lead to new analytical techniques in an SEM, such as glow discharge optical emission spectroscopy (GDOES),[55,56] where the emission from sputtered material in a plasma is studied while ablating the sample material for depth profiling (similar to secondary ion mass spectroscopy in focused ion beam instruments).[57] On the other hand, established (e.g., EDS or wavelength dispersive X-ray spectroscopy, WDS)[58] or more recently available (e.g., electron energy loss spectroscopy, EELS)[59] analytical methods in SEMs may have the potential to probe the ionic species in the plasma cloud. This would provide essential and direct in-situ feedback for plasma simulation codes and holds promise for improved control over plasma setups.

3. Conclusions

A custom-built microplasma setup was realized inside an SEM based on the design by Matra et al.[13] A nozzle with a small orifice feeds a gas into the evacuated SEM chamber, from which a plasma can be generated by applying a certain electrical potential. Stable DC glow discharge plasmas with Ar, Ar/O_2, CO_2, and N_2 gases were successfully generated in the SEM's vacuum chamber. In general, larger discharge currents were measured for higher gas flow rates and smaller gap distances. A non-uniform gas-pressure profile was observed in the plasma gap, which—in combination with a non-uniform electric field of the electrode geometry—complicates a direct comparison of the shown setup with conventional plasma systems. Simultaneous SEM imaging with SEs and BSEs during plasma operation

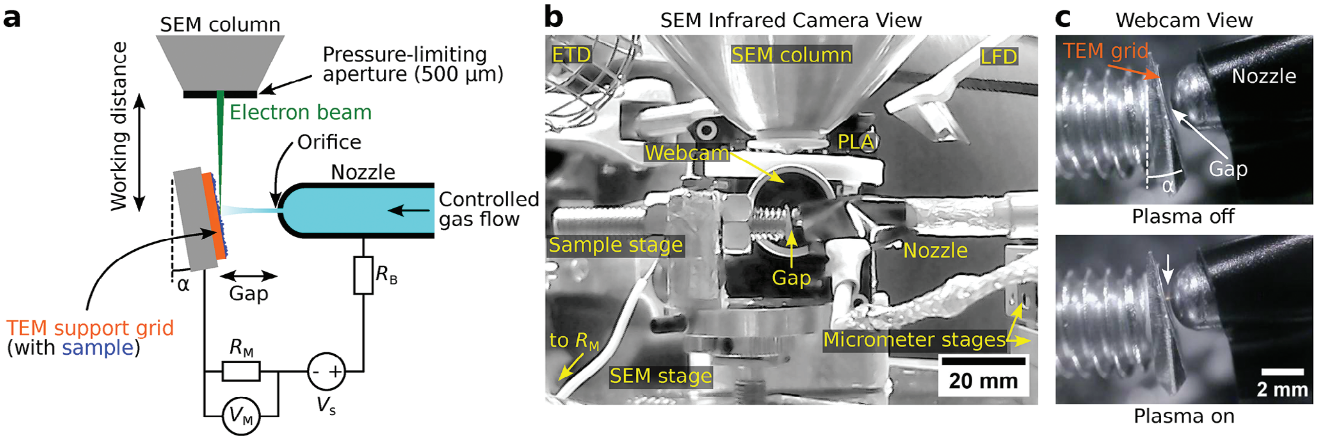

Figure 9. Schematics and images of the plasma-in-SEM setup. a) Schematic showing the experimental setup and the most important components. Gas flows from a nozzle orifice over an adjustable gap distance toward a sample surface. A high voltage V_S is applied to ignite the plasma. The sample surface is slightly tilted at an angle α toward the SEM incidence, allowing for in situ SEM imaging. b) Image of the setup taken with the built-in infrared camera of the SEM showing the setup. A few additional components are shown compared to (a), such as a webcam and the electron detectors, ETD and LFD. c) Higher-magnification side-view of the plasma region using the webcam without plasma (upper) and with ignited plasma (lower, the microplasma is marked with an arrow).

was demonstrated, enabling in-situ studies of sample-plasma interactions in the SEM.

A few exemplary plasma-sample interactions were studied. Sputtering of Cu surfaces and Ni nanoparticles under different gases was observed. The lower sputter yield of the Ni particles compared to the Cu support, as well as the incidence-angle dependence of the sputter yield, results in the local formation of cones in the plasma-treated area. The same phenomenon was studied with conventional plasma reactors, which shows that our setup can replicate such experimental conditions on the local scale of several tens of µm. Local oxidation of Cu and Ni was observed for CO_2 gas and an Ar/O_2 gas mixture. At the same time, however, the sample was either simultaneously sputtered away by ion bombardment on the sample, or nozzle material was redeposited on the sample by sputtering of the nozzle. These limitations might be overcome by further optimizations of the setup, though for applications where sputtering is detrimental, other types of plasma are to be considered.

In conclusion, we have demonstrated that in-situ studies of plasma-sample interactions in a modern SEM are possible. This approach provides direct insight into morphological and chemical changes (via EDS) of the sample during and after plasma treatment. Overall, this may lead to a better understanding of plasma physics and plasma-surface interactions.

4. Experimental

SEM Operation with the Plasma Setup: Plasma experiments were performed using an FEI Quanta 250 ESEM equipped with an Oxford Instruments X-Max EDS detector (80 mm^2 sensor area). **Figure** 9a schematically shows the main parts of the plasma setup that was built in-house. A horizontally aligned steel nozzle with a small orifice (SS-1/8-TUBE-CAL-20, 20 µm nominal orifice diameter, Lenox Laser) was fixed opposite to a nearly vertically aligned sample surface. The sample surface was slightly tilted with an angle $\alpha \approx 10°$ toward the electron beam for better SEM imaging conditions. The sample-nozzle distance ("Gap" in Figure 9a–c) determined the plasma gap distance and could be adjusted by moving the sample with SEM microscope stage controls. A gas flowed from the nozzle into the gap toward the sample surface. The nozzle could be biased with a DC voltage V_S in the range of -1.25 to 2 kV, that is, with a positive or negative polarity relative to the sample. A ballast resistance $R_B = 4.3\ \text{M}\Omega$ was used to limit the discharge current. The discharge current $I_D = V_M/R_M$ was measured by the voltage drop V_M across a $R_M = 1\ \text{k}\Omega$ resistor.

Figure 9b displays the experimental setup with an image taken with the microscope's built-in infrared (IR) camera. A few additional components compared to the schematic in Figure 9a are visible, which are explained from top to bottom in the following. The ETD and the large-field detector (LFD) were used for SEM imaging in high-vacuum and low-vacuum modes, respectively. The images shown in this work were mainly SE-SEM images. Selected BSE-SEM images were mentioned explicitly in the text. A pressure-limiting aperture (PLA) with a 500 µm diameter was mounted on the SEM pole piece to restrict gas flow into the microscope column. An IR-USB webcam (Arducam B0205) was mounted in addition to the microscope's built-in IR camera to improve imaging conditions of the plasma and control the gap distance. The sample stage consisted of a threaded metal rod that was rigidly fixed with two nuts to a Teflon piece. The Teflon piece isolated the sample from the microscope stage to prevent current flow through the latter and possible damage to the microscope. Instead, the current flows via a cable to the measurement resistor R_M. The sample stage with the threaded metal rod and the Teflon block were fixed on an SEM stub, which itself was fixed on the moveable SEM stage. Two micrometer stages (Thorlabs MS3/M) were used to laterally position the nozzle close to the optical axis (below the SEM pole piece) before closing the SEM chamber. The nozzle and the webcam were mounted on an Al platform that was fixed above the moving microscope stage. The height of the Al platform could be adjusted to change the working distance between the SEM column and the sample (typically 15 mm). The gas line and electrical connections were routed through a custom home-made feedthrough flange.

A detailed image of the plasma gap is shown in the webcam view (Figure 9c). Commercially available grids or apertures made for transmission electron microscopy (TEM) with a 3 mm diameter (Gilder Grids GA50 Cu apertures) were typically used as sample or sample support for nanoparticles. The sample was mounted on an Al wedge with conductive Ag paste (EM-Tec AG15). The Al wedge was ground at an angle α and fixed to the threaded metal rod's end with conductive Ag paste. The lower image in Figure 9c shows the working setup with a glowing DC microplasma. More details about the experimental setup can be found in the Supporting Information (Figure S8, Supporting Information).

Plasma Operation: Plasma experiments were performed in the high-vacuum mode of the microscope since undesired discharges in the SEM chamber in low-vacuum mode were observed when applying high voltage between the nozzle and the sample. The high-vacuum mode reached a stable chamber pressure of around 2×10^{-2} Pa while providing a gas flow of about 2 to 8 sccm through the nozzle (20 µm nominal orifice diameter as per the manufacturer) into the microscope chamber. The gas flow was monitored using an Alicat flow meter (M-200SCCM-D/5M). CO_2 (purity 99.995%), Ar (99.9999%), and N_2 (99.9999%) gases, and a 75%Ar/25%O_2 gas mixture (measured: 74.88%/25.12%) were used in this work (bought from Air Products).

The plasma was operated by applying and controlling the voltage difference on the nozzle relative to the sample. A DC–DC converter with a 1 MΩ output resistor (CA20P or CA12N depending on polarity, XP Power) was powered by an RS PRO IPS-3303 power supply. The 1 MΩ output resistor limited the output current of the DC–DC converter in standalone usage for user safety. The output resistor was in series with a 3.3 MΩ resistor, resulting in a total ballast resistance $R_B = 4.3$ MΩ. The output high voltage V_S of the DC–DC converter was adjusted with a control voltage between 0 and 5 V using a Keysight E36106B power supply. After plasma ignition, the discharge current was regulated by adjusting V_S with the control voltage. Voltage–current characteristics of the plasma were measured with a Keithley 2400 source measurement unit. The highest source voltage of 2 kV was applied, after which the source voltage was gradually reduced while registering the current until no discharge current was measurable. The discharge voltage of the DC plasma V_D is calculated as $V_D = V_S - I_D(R_B + R_M)$.[6]

Sample Preparation: A Cu TEM aperture (50 µm, Gilder Grids GA50) with a diameter of 3 mm and a thickness of about 30 µm was used in most experiments to ensure a well-defined, flat electrode opposing the nozzle. For experiments with nanoparticles, commercial Ni particles (nanopowder, <100 nm nominal average particle size, >99% purity, Sigma-Aldrich, CAS number 7440-02-0) were mixed with acetone and then drop cast on the Cu disc. After solvent evaporation, a thin film of Ni particles was left on the Cu surface. Drop casting was repeated multiple times until the TEM aperture was fully covered with Ni particles.

Data Processing: *Fiji*[60] was used for general image processing. Images were stitched together using the "Grid/collection stitching" plugin.[61] Image series were registered using the "Descriptor-based series registration (2d/3d + t)" plugin.[62] The background-corrected X-ray peak intensities (net intensities) for the EDS maps were extracted using the "TruMap" function in the Oxford Instruments *AZtec* software (version 2.1). Additional analyses of extracted (summed-up) EDS spectra from specific regions were processed with the *HyperSpy* Python package.[63]

Supporting Information

Supporting Information is available from the Wiley Online Library or from the author.

Acknowledgements

L.G., S.B., and J.V. acknowledge support from the iBOF-21-085 PERsist research fund. D.C., S.V.A., and J.V. acknowledge funding from a TOP-BOF project of the University of Antwerp (FFB 170366). R.D.M., A.B., and J.V. acknowledge funding from the Methusalem project of the University of Antwerp (FFB 15001A, FFB 15001C). A.O. and J.V. acknowledge funding from the Research Foundation Flanders (FWO, Belgium) project SBO S000121N.

Conflict of Interest

The authors declare no conflict of interest.

Author Contributions

L.G., D.C., and R.D.M. contributed equally to this work. L.G.: Conceptualization, methodology, investigation, software, validation, formal analysis, data curation, visualization, writing—original draft. D.C.: Conceptualization, methodology, investigation, writing—review and editing. R.D.M.: Conceptualization, methodology, investigation, validation, writing—original draft. A.O.: Conceptualization, methodology, writing—review and editing. S.V.A.: Conceptualization, supervision, project administration, funding acquisition, writing—review and editing. A.B.: Conceptualization, supervision, project administration, funding acquisition, writing—review and editing. S.B.: Conceptualization, supervision, project administration, funding acquisition, writing — review and editing. J.V.: Conceptualization, methodology, supervision, project administration, funding acquisition, Writing — review and editing.

Data Availability Statement

The data that support the findings of this study are openly available in Zenodo at https://doi.org/10.5281/zenodo.8042029 , reference number 8042029.[64]

Keywords

energy-dispersive X-ray spectroscopy, environmental scanning electron microscopy, in situ scanning electron microscopy, microplasma, plasma, scanning electron microscopy, sputtering

Received: September 26, 2023
Revised: January 15, 2024

[1] K. J. Kanarik, *J. Vac. Sci. Technol., A* **2020**, *38*, 031004.
[2] M. Laroussi, *IEEE Trans. Plasma Sci.* **2015**, *43*, 703.
[3] L. Lin, Q. Wang, *Plasma Chem. Plasma Process.* **2015**, *35*, 925.
[4] A. Bogaerts, E. Neyts, R. Gijbels, J. van der Mullen, *Spectrochim. Acta, Part B* **2002**, *57*, 609.
[5] A. A. Fridman, L. A. Kennedy, *Plasma Physics and Engineering*, 2nd ed., CRC Press, Boca Raton, FL **2011**.
[6] J. T. Gudmundsson, A. Hecimovic, *Plasma Sources Sci. Technol.* **2017**, *26*, 123001.
[7] W.-H. Chiang, D. Mariotti, R. M. Sankaran, J. G. Eden, K. K. Ostrikov, *Adv. Mater.* **2020**, *32*, 1905508.
[8] K. H. Schoenbach, K. Becker, *Eur. Phys. J. D* **2016**, *70*, 29.
[9] F. Iza, G. J. Kim, S. M. Lee, J. K. Lee, J. L. Walsh, Y. T. Zhang, M. G. Kong, *Plasma Processes Polym.* **2008**, *5*, 322.
[10] R. Foest, M. Schmidt, K. Becker, *Int. J. Mass Spectrom.* **2006**, *248*, 87.
[11] V. Karanassios, *Spectrochim. Acta, Part B* **2004**, *59*, 909.
[12] X. Lu, M. Laroussi, V. Puech, *Plasma Sources Sci. Technol.* **2012**, *21*, 034005.
[13] K. Matra, Y. Mizobuchi, H. Furuta, A. Hatta, *Vacuum* **2013**, *87*, 132.
[14] J. Mulders, P. Trompenaars, in *Proc. of European Microscopy Congress 2016*, John Wiley & Sons, Ltd, Hoboken, NJ **2016**, pp. 453–454.
[15] K. Pardinas, *Ph.D. Thesis*, Princeton University, NJ **2016**.
[16] D. Phifer, L. Tuma, T. Vystavel, P. Wandrol, R. J. Young, *Microsc. Today* **2009**, *17*, 40.
[17] J. Jiruše, M. Havelka, F. Lopour, *Ultramicroscopy* **2014**, *146*, 27.
[18] R. Isaacs, A. Prokhodtseva, T. Vystavel, *Microsc. Microanal.* **2018**, *24*, 1060.
[19] M. Dutka, R. Isaacs, A. Prokhodtseva, T. Vystavěl, *Microsc. Microanal.* **2019**, *25*, 548.

[20] G. D. Danilatos, in *Advances in Electronics and Electron Physics* (Ed.: P. W. Hawkes), Vol. *71*, Academic Press, Cambridge, MA **1988**, pp. 109–250.
[21] J. I. Goldstein, D. E. Newbury, J. R. Michael, N. W. Ritchie, J. H. J. Scott, D. C. Joy, *Scanning Electron Microscopy and X-Ray Microanalysis*, Springer, New York, NY **2018**.
[22] K. Matra, H. Furuta, A. Hatta, *J. Phys.: Conf. Ser.* **2013**, *441*, 012021.
[23] K. Matra, Ph.D. Thesis, Kochi University of Technology, Kochi, Japan **2013**.
[24] K. Matra, H. Furuta, A. Hatta, *Micromachines* **2017**, *8*, 211.
[25] E. P. Muntz, S. J. Abel, B. L. Maguire, *IEEE Trans. Aerosp.* **1965**, *AS-3*, 210.
[26] F. Sharipov, *J. Fluid Mech.* **2004**, *518*, 35.
[27] S. Misdanitis, S. Pantazis, D. Valougeorgis, *Vacuum* **2012**, *86*, 1701.
[28] N. Y. Bykov, V. V. Zakharov, *Phys. Fluids* **2020**, *32*, 067109.
[29] F. Salehi, A. J. Goers, L. Feder, B. Miao, D. Woodbury, H. M. Milchberg, *Rev. Sci. Instrum.* **2019**, *90*, 103001.
[30] M. Patel, J. Thomas, H. C. Joshi, *Vacuum* **2021**, *192*, 110440.
[31] V. A. Lisovskiy, S. D. Yakovin, V. D. Yegorenkov, *J. Phys. D: Appl. Phys.* **2000**, *33*, 2722.
[32] V. A. Lisovskiy, R. O. Osmayev, A. V. Gapon, S. V. Dudin, I. S. Lesnik, V. D. Yegorenkov, *Vacuum* **2017**, *145*, 19.
[33] P. Mathew, J. George, S. Mathews T, P. J. Kurian, *AIP Adv.* **2019**, *9*, 025215.
[34] Y. Fu, P. Zhang, J. P. Verboncoeur, X. Wang, *Plasma Res. Express* **2020**, *2*, 013001.
[35] D. J. Stokes, Environmental scanning electron microscroscopy for biology and polymer science, https://analyticalscience.wiley.com/content/article-do/environmental-scanning-electron-microscopy-biology-and-polymer-science, (accessed: February 2024).
[36] V. Neděla, E. Tihlaříková, J. Runštuk, J. Hudec, *Ultramicroscopy* **2018**, *184*, 1.
[37] A. Güntherschulze, W. Tollmien, *Z. Phys.* **1942**, *119*, 685.
[38] O. Auciello, *J. Vac. Sci. Technol.* **1981**, *19*, 841.
[39] G. K. Wehner, *J. Vac. Sci. Technol., A* **1985**, *3*, 1821.
[40] A. van Teijlingen, S. A. Davis, S. R. Hall, *Nanoscale Adv.* **2020**, *2*, 2347.
[41] C. Pabari, *Mater. Today: Proc.* **2022**, *55*, 98.
[42] A. D. G. Stewart, M. W. Thompson, *J. Mater. Sci.* **1969**, *4*, 56.
[43] V. I. Shulga, *Appl. Surf. Sci.* **2018**, *439*, 456.
[44] Z. Wang, Y. Zhang, E. C. Neyts, X. Cao, X. Zhang, B. W.-L. Jang, C.-j. Liu, *ACS Catal.* **2018**, *8*, 2093.
[45] Z. Ye, L. Zhao, A. Nikiforov, J.-M. Giraudon, Y. Chen, J. Wang, X. Tu, *Adv. Colloid Interface Sci.* **2022**, *308*, 102755.
[46] D. Serafin, W. J. Nowak, B. Wierzba, *Appl. Surf. Sci.* **2019**, *476*, 442.
[47] P. Song, D. Wen, Z. X. Guo, T. Korakianitis, *Phys. Chem. Chem. Phys.* **2008**, *10*, 5057.
[48] R. Sainju, D. Rathnayake, H. Tan, G. Bollas, A. M. Dongare, S. L. Suib, Y. Zhu, *ACS Nano* **2022**, *16*, 6468.
[49] S. Kunze, L. C. Tănase, M. J. Prieto, P. Grosse, F. Scholten, L. d. S. Caldas, D. van Vörden, T. Schmidt, B. R. Cuenya, *Chem. Sci.* **2021**, *12*, 14241.
[50] Y. Xia, P. Sautet, *ACS Nano* **2022**, *16*, 20680.
[51] G. Willems, A. Hecimovic, K. Sgonina, E. Carbone, J. Benedikt, *Plasma Phys. Controlled Fusion* **2020**, *62*, 034005.
[52] A. Bogaerts, X. Tu, J. C. Whitehead, G. Centi, L. Lefferts, O. Guaitella, F. Azzolina-Jury, H.-H. Kim, A. B. Murphy, W. F. Schneider, T. Nozaki, J. C. Hicks, A. Rousseau, F. Thevenet, A. Khacef, M. Carreon, *J. Phys. D: Appl. Phys.* **2020**, *53*, 443001.
[53] Th. von Woedtke, S. Reuter, K. Masur, K. D. Weltmann, *Phys. Rep.* **2013**, *530*, 291.
[54] F. Massines, N. Gherardi, N. Naudé, P. Ségur, *Eur. Phys. J.: Appl. Phys.* **2009**, *47*, 22805.
[55] W. Grimm, *Spectrochim. Acta, Part B* **1968**, *23*, 443.
[56] G. Gamez, M. Voronov, S. J. Ray, V. Hoffmann, G. M. Hieftje, J. Michler, *Spectrochim. Acta, Part B* **2012**, *70*, 1.
[57] L. Pillatsch, F. Östlund, J. Michler, *Prog. Cryst. Growth Charact. Mater.* **2019**, *65*, 1.
[58] X. Llovet, A. Moy, P. T. Pinard, J. H. Fournelle, *Prog. Mater. Sci.* **2021**, *116*, 100673.
[59] N. Brodusch, H. Demers, A. Gellé, A. Moores, R. Gauvin, *Ultramicroscopy* **2019**, *203*, 21.
[60] J. Schindelin, I. Arganda-Carreras, E. Frise, V. Kaynig, M. Longair, T. Pietzsch, S. Preibisch, C. Rueden, S. Saalfeld, B. Schmid, J.-Y. Tinevez, D. J. White, V. Hartenstein, K. Eliceiri, P. Tomancak, A. Cardona, *Nat. Methods* **2012**, *9*, 676.
[61] S. Preibisch, S. Saalfeld, P. Tomancak, *Bioinformatics* **2009**, *25*, 1463.
[62] S. Preibisch, S. Saalfeld, J. Schindelin, P. Tomancak, *Nat. Methods* **2010**, *7*, 418.
[63] F. de la Peña, E. Prestat, V. T. Fauske, P. Burdet, J. Lähnemann, P. Jokubauskas, T. Furnival, M. Nord, T. Ostasevicius, K. E. MacArthur, D. N. Johnstone, M. Sarahan, J. Taillon, T. Aarholt, pquinn-dls, V. Migunov, A. Eljarrat, J. Caron, C. Francis, T. Nemoto, T. Poon, S. Mazzucco, actions-user, N. Tappy, N. Cautaerts, S. Somnath, T. Slater, M. Walls, F. Winkler, H. W. Ånes, *Hyperspy/hyperspy: Release v1.7.3*, Zenodo, **2022**, DOI: https://10.5281/zenodo.7263263.
[64] L. Grünewald, D. Chezganov, R. De Meyer, A. Orekhov, S. Van Aert, A. Bogaerts, S. Bals, J. Verbeeck, *arXiv:2308.15123v1*, **2023**, pp. 21–29.